

## Article

# Making the Most of 3D Electron Diffraction: Best Practices to Handle a New Tool

Khai-Nghi Truong <sup>1,†</sup> , Sho Ito <sup>2,3,†</sup>, Jakub M. Wojciechowski <sup>1</sup> , Christian R. Göb <sup>1</sup> , Christian J. Schürmann <sup>1</sup>, Akihito Yamano <sup>2</sup>, Mark Del Campo <sup>4</sup> , Eiji Okunishi <sup>5</sup>, Yoshitaka Aoyama <sup>5</sup>, Tomohiro Mihira <sup>5</sup>, Naoki Hosogi <sup>5</sup>, Jordi Benet-Buchholz <sup>6</sup>, Eduardo Carmelo Escudero-Adán <sup>6</sup> , Fraser J. White <sup>1</sup>, Joseph D. Ferrara <sup>4</sup> , and Robert Buecker <sup>1,\*</sup> 

<sup>1</sup> Rigaku Europe SE, Hugenottenallee 167, 63263 Neu-Isenburg, Germany

<sup>2</sup> Rigaku Corporation, 3-9-12 Matsubara, Akishima 196-8666, Japan

<sup>3</sup> DIC Central Research Laboratories, 631, Sakado, Sakura 285-8668, Japan

<sup>4</sup> Rigaku Americas Corporation, 9009 New Trails Drive, The Woodlands, TX 77381, USA

<sup>5</sup> JEOL Ltd., 3-1-2 Musashino, Akishima 196-8558, Japan

<sup>6</sup> Institute of Chemical Research of Catalonia (ICIQ), The Barcelona Institute of Science and Technology, Av. Paisos Catalans 16, 43007 Tarragona, Spain

\* Correspondence: robert.buecker@rigaku.com

† These authors contributed equally to this work.

**Abstract:** Along with the adoption of three-dimensional electron diffraction (3D ED/MicroED) as a mainstream tool for structure determination from sub-micron single crystals, questions about best practices regarding each step along the workflow, from data collection to structure solutions, arise. In this paper, we discuss three particular aspects of a 3D ED/MicroED experiment which, after hundreds of structures solved in Rigaku's laboratories, we have found to be important to consider carefully. First, for a representative model system of a hydrated compound (trehalose dihydrate), we show that cryo-transfer of the sample into the diffractometer is an effective means to prevent dehydration, while cooling of the sample without cryo-transfer yields a marginal improvement only. Next, we demonstrate for a small (tyrosine) and a large (clarithromycin) organic compound, how a simplified and fast workflow for dynamical diffraction calculations can determine absolute crystal structures with high confidence. Finally, we discuss considerations and trade-offs for choosing an optimal effective crystal-to-detector distance; while a long distance is mandatory for a protein (thaumatin) example, even a small molecule with difficult diffraction behavior (cystine) yields superior results at longer distances than the one used by default.

**Keywords:** electron diffraction; 3D ED; MicroED; single crystal diffraction; structure determination; absolute structure; cryo-transfer; crystallography; instrumentation



**Citation:** Truong, K.-N.; Ito, S.; Wojciechowski, J.M.; Göb, C.R.; Schürmann, C.J.; Yamano, A.; Del Campo, M.; Okunishi, E.; Aoyama, Y.; Mihira, T.; et al. Making the Most of 3D Electron Diffraction: Best Practices to Handle a New Tool. *Symmetry* **2023**, *15*, 1555. <https://doi.org/10.3390/sym15081555>

Academic Editors: Partha Pratim Das, Arturo Ponce-Pedraza, Enrico Mugnaioli and Stavros Nicolopoulos

Received: 7 June 2023

Revised: 2 August 2023

Accepted: 4 August 2023

Published: 8 August 2023



**Copyright:** © 2023 by the authors. Licensee MDPI, Basel, Switzerland. This article is an open access article distributed under the terms and conditions of the Creative Commons Attribution (CC BY) license (<https://creativecommons.org/licenses/by/4.0/>).

## 1. Introduction

Crystal structure determination using electron diffraction has seen an unprecedented revival starting from the late 2000s, sparked by the introduction of new data collection methods. These methods are analogous to single-crystal X-ray crystallography, wherein three-dimensional datasets are collected by stepwise or continuous rotation of single crystals in the probe beam without alignment to specific zone axes. These approaches are now commonly referred to under the umbrella terms 3D ED and MicroED [1–6]. The ability to obtain structures from single crystals in the sub-micron size range has generated huge interest in a wide range of scientific communities in organic and inorganic chemistry, as well as structural biology. Excellent review papers have recently become available, to which we would like to direct the reader for further introduction to the history, scope, and applications of 3D ED [6–9].

Hitherto, 3D ED has been performed in transmission electron microscopes (TEMs) which have typically been augmented by specific data collection software and/or hardware extensions such as precession units or dedicated diffraction detectors. More recently, dedicated electron diffractometers have become commercially available [10,11], which eliminate the requirement of prior skill in TEM operation and offer a user experience and workflows closely resembling those of single-crystal X-ray diffractometers. As such, 3D ED can be seamlessly integrated into the portfolio of crystallographic facilities. Despite their relatively recent introduction, dedicated electron diffractometers have already contributed significantly to published 3D ED studies from various fields [12–23]. Here, we specifically make use of the Rigaku XtaLAB Synergy-ED diffractometer [10], the central design principle of which is the complete integration of the collection, data processing, and structure solution process. The operational interface and user experience match that of Rigaku Oxford Diffraction X-ray diffractometers, driven by the fully integrated software package CrysAlis<sup>Pro</sup> [24]. The electron optics of the XtaLAB Synergy-ED are based on a 200 kV electron gun with a lanthanum hexaboride crystal as the electron emitter. They were developed in collaboration with JEOL Ltd., based on JEOL's established platform for TEMs, specifically regarding the gun optics, the mechanical design, and the fully automated vacuum system. Notably, the goniometer of the XtaLAB Synergy-ED, despite some modifications to optimize performance for 3D ED, remains compatible with the wide portfolio of sample holders available for TEMs, such as cryo-transfer systems, as discussed below.

In this paper, based on lessons learned from more than 380 structures solved on XtaLAB Synergy-ED diffractometers in our application laboratories, we will discuss considerations for obtaining high-quality small-molecule and protein structures regarding sample cooling and cryo-transfer, radiation dose, crystal-to-detector distance, and absolute structure determination through dynamical refinement.

## 2. Materials and Methods

All small-molecule samples were commercially available, obtained in powder form, and used without further modification. Trehalose was purchased as both the dihydrate and anhydrous forms (>98% purity) from Tokyo Chemical Industry Germany GmbH (Eschborn, Germany). Clarithromycin (>99.5% purity) was purchased from LKT Laboratories (St. Paul, MN, USA), Inc. L-Tyrosine (>99% purity) was purchased from FUJIFILM Wako Pure Chemical Corporation (Osaka, Japan). Cystine was purchased from CARL ROTH ( $\geq$ 98.5% purity, Karlsruhe, Germany).

### 2.1. Sample Grid Preparation

For small-molecule experiments, the microcrystalline powders were directly applied to continuous or lacey-carbon TEM grids after gentle grinding of sample powder between glass slides in order to break up larger crystals and agglomerates.

Thaumatococcus protein crystals were grown by batch crystallization from a 50 mg/mL solution in 100 mM ADA buffer (pH 6.5) by the addition of 1.5 M potassium sodium tartrate (pH 7.0) at a volume ratio of 1:1 at 20 °C. Next, 4  $\mu$ L aliquots were applied to glow-discharged holey-carbon-coated copper grids at room temperature, blotted, and plunge-frozen into liquid ethane using a Leica GP2 plunger. One of the prepared sample grids was transferred to a Gatan Elsa (Model 698) cryo-transfer holder and introduced into a JEOL JIB-4000PLUS focused ion beam mill for further thinning [25]. Thin lamellae were cut out of 10 crystals using a gallium ion beam of successively lower currents (1 nA, 350 pA, 23 pA) down to approximately 250 nm thickness which is close to the optimal thickness for 3D ED [26,27]. The milling process took approximately 20 min per crystal on average. The grid was then directly cryo-transferred while remaining on the sample holder into the diffractometer for data collection.

## 2.2. Data Collection

All data collection was performed on identical Rigaku XtaLAB Synergy-ED diffractometers [10] located at various sites. Diffraction data are collected using an integrated Rigaku HyPix-ED hybrid-pixel detector ( $775 \times 385$  pixels,  $(100 \mu\text{m})^2$  pixel size, frame rate up to 130 Hz) in zero dead time mode. Due to the event counting capability of the detector, readout and dark noise are not observed, ensuring the detectability of single electrons and no constraints in the choice of scan widths. The XtaLAB Synergy-ED diffractometer is fully controlled by the Rigaku Oxford Diffraction CrysAlis<sup>Pro</sup> program package [24], which, in addition to real-space screening and data collection (instant and queued), also performs integrated on-the-fly and off-line data processing. Additionally, automatic structure solution and refinement for small molecules are possible within CrysAlis<sup>Pro</sup> using AutoChem [28]. JEOL tomography-retainer and Gatan Elsa (Model 698) cryo-transfer sample holders were used for room-temperature and cryogenic measurements, respectively.

After insertion of a sample grid into the diffractometer, it is inspected in real space using the diffractometer's *visual mode*. First, a very low-resolution image covering the entire grid for coarse navigation is taken (*minimap*). Next, interactive screening is performed using *video-mode* or *snapshot-mode* visualization at a suitable magnification for identifying grains with morphological properties optimal for electron diffraction. For typical organic compounds or proteins as studied in this work, a crystal thickness of the order of 500 nm along the directions covered by the rotation scan is desirable for an optimal trade-off between signal strength and reasonable levels of background due to inelastic scattering. An extremely low electron flux (dose rate) of the order of  $5 \times 10^{-4} \text{ e}^- / (\text{\AA}^2 \cdot \text{s})$  is used for screening to prevent radiation damage before data collection. Diffraction snapshots of candidates can be immediately collected, or grain positions can be queued for automatic screening, similar to existing workflows for 3D ED [29–31]. For each grain that is found to be well-diffracting, centering along the beam propagation direction is performed using a semi-automatic point-and-click interface. Afterward, data collection can either be immediately started or queued for unattended collection. All data collections are performed in shutterless continuous-rotation mode [4,6] at scan speeds of typically  $0.5\text{--}3 \text{ s}/^\circ$  and fluxes of  $1 \times 10^{-3}$  to  $5 \times 10^{-3} \text{ e}^- / (\text{\AA}^2 \cdot \text{s})$ . A selected-area aperture of  $1 \mu\text{m}$  or  $2 \mu\text{m}$  apparent diameter (imaged on the sample plane) is used for isolation of the diffraction signal from the chosen grain. During data collection, unit cell determination and data reduction are continuously performed on-the-fly in CrysAlis<sup>Pro</sup>, and online structure solution and refinement using AutoChem are started once data completeness passes a preset threshold.

For all small-molecule datasets, diffraction data were typically collected over wedges of  $90\text{--}125^\circ$  at total radiation doses (fluence) of  $0.1\text{--}10 \text{ e}^- / \text{\AA}^2$  per run (see Supplementary Crystallographic Tables for details). For thaumatin, diffraction data were collected over a total range of  $70^\circ$  from one of the crystals with a total dose of  $10 \text{ e}^- / \text{\AA}^2$ .

## 2.3. Data Processing and Structure Solution

For all datasets, indexing, integration, and space-group determination were performed using CrysAlis<sup>Pro</sup> 43.49a (L-tyrosine, clarithromycin) or 43.70a (thaumatin, trehalose, cystine). For small-molecule datasets, after dataset scaling and merging in CrysAlis<sup>Pro</sup>, crystal structures were solved using direct methods and refined in the kinematical approximation in Olex2, using SHELXT [32] and SHELXL [33] as respective back-ends. For some datasets, the extinction parameter (EXTI) was used in refinement to prevent negative anisotropic displacement factors (ADPs) [34]. Further dynamical refinement using Jana2020 [35,36] was performed on some datasets, as will be discussed below. For thaumatin, after the export of unmerged data and subsequent merging using AIMLESS [37], molecular-replacement phasing was performed using PHASER [38]. Multiple rounds of model building with Coot 0.9.8 [39] and refinement with REFMAC5 [40] were performed until arriving at a completed model with satisfactory R-factors and geometry. Note that sum of Gaussian electron scattering factors was used in REFMAC5.

### 3. Results

In this section, we will discuss results from measurements on typical test samples that address three key aspects of experiment design unique to 3D ED: (i) the need to keep hydration/solvation of the specimen under vacuum; (ii) crystal structure refinement using dynamical diffraction calculations; and (iii) selection of appropriate crystal-to-detector distance using electron optics.

#### 3.1. Preservation and Dehydration of Trehalose Dihydrate

As in X-ray crystallography, cooling the samples during an electron diffraction experiment [41] can significantly enhance data quality in terms of diffraction resolution and completeness through reduced thermal motion giving rise to an increase in scattering power. In electron diffraction, however, beam damage is generally a larger concern but can be mitigated to an extent with the help of low temperatures providing a longer lifetime of the crystal while in the beam. For a broad range of samples, in our laboratories, we often observe a similar behavior for electron diffraction, such that the time overhead for cooling the sample is more than offset by the faster screening for well-diffracting grains and lower requirements for careful dose optimization. A very different and even more crucial use case for cryo-preservation arises for samples such as hydrated and solvent-containing compounds, co-crystals, or proteins, where exposure to vacuum would lead to loss of hydration or solvent [17,23], often even leading to an entire collapse of the crystal lattice. For such samples, dehydration occurs quickly after transfer into the diffractometer, so simple cooling of the sample stage is not sufficient protection, and cryo-transfer, whereby the sample is frozen outside the vacuum and transferred into the diffractometer using a suitable cryo-transfer holder, is required.

As a representative organic molecule illustrating the typically observed behavior of hydrated small-molecule compounds, we studied the case of trehalose dihydrate, comparing results from ED experiments obtained at room temperature, at liquid-nitrogen temperature, and using cryo-transfer. We will compare the results to the case of natively anhydrous trehalose.

First, we introduced a sample grid of trehalose dihydrate into the diffractometer at room temperature. Among ~20 grains chosen for screening by their morphological properties (like grains shown in Figure 1g), most exhibited no diffraction or only very poor diffraction; only 3 grains were found suitable for data collection at an ultra-low total dose of  $0.16 \text{ e}^- / \text{\AA}^2$  and structure solution. In Figure 1b, a screening image, a representative diffraction frame, and the refined structure from one of those grains are shown. Full dehydration of the crystal due to exposure to the diffractometer vacuum was found for all grains. We then cooled down the sample to 100 K while keeping it in the vacuum environment of the diffractometer and repeated the measurement on the same grain to obtain a dataset with marginally improved statistics (Figure 1c, Table S1 in Supplementary Materials). Finally, we repeated the measurement with a total dose three times higher, which led to a further improvement in data refinement quality, specifically with regard to the signal-to-noise ratio (Table S1). For all datasets, we found an orthorhombic unit cell with volume  $\approx 1450 \text{ \AA}^3$  and a space group  $P2_12_12_1$ , matching a polymorph of anhydrous trehalose which has previously been described in the literature to arise from direct dehydration of trehalose dihydrate [42].

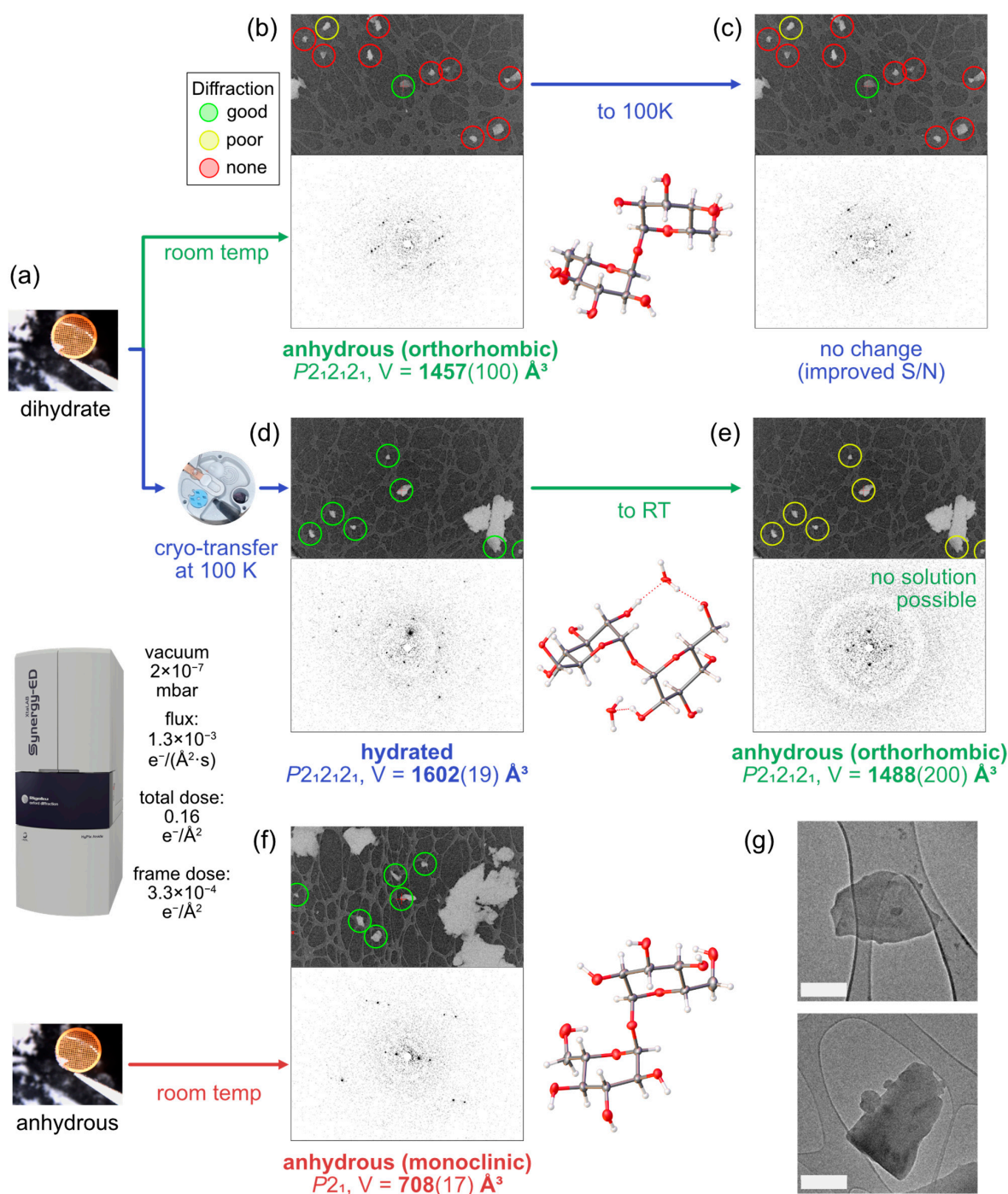


**Figure 1.** Dehydration and preservation of trehalose dihydrate inside the diffractometer. (a) Grids with powder of trehalose dihydrate (top) or anhydrous trehalose (bottom) are loaded on lacey-carbon coated copper grids and loaded into the diffractometer at either room temperature or at 100 K, using a cryo-transfer system; 3D ED datasets are taken at ultra-low dose to minimize the impact of radiation damage on our findings. (b) Typical screening result, diffraction pattern, and structure solution of anhydrous trehalose found after dehydration of the dihydrate in vacuum. Green, yellow, and red circles in the screening images indicate well-diffracting, poorly diffracting, and non-diffracting crystals, respectively. (c) Data from the same crystal in (b), after cooling to 100 K inside the vacuum. (d) Result for a grid with dihydrates preserved by cryo-transfer. (e) Data from the same crystal in (d), after warming up to room temperature inside the vacuum. (f) Result for a grid containing specifically prepared anhydrous trehalose, transferred into vacuum at room temperature. (g) Close-up real-space images of two typical grains taken after data collection. Scale bars correspond to 500 nm.

In the case of cryo-transferred trehalose dihydrate, we found good diffraction from all inspected morphologically suitable grains. The unit cell matched an orthorhombic cell with a slightly bigger volume of  $1602(19) \text{ \AA}^3$  than that of the anhydrous form, again in accordance with the literature [42,43]. We collected diffraction data from seven such grains at an ultra-low radiation dose of  $0.16 \text{ e}^- / \text{ \AA}^2$  each, all of which led to a structure solution containing the two co-crystallized water molecules as shown in Figure 1d, unambiguously demonstrating the ability to preserve hydration. Due to the rather high-symmetry point group, a dataset of sufficient completeness could be collected from a single grain. After collecting the dihydrate crystal data, we warmed up the sample to ambient temperature while it remained in the vacuum environment of the diffractometer's airlock chamber. Revisiting the grains from which each data set was collected showed no visible morphological changes; however, only weak, low-resolution diffraction data could be obtained (Figure 1e). While data quality was too low for structure solution, we could determine the unit cells of the checked crystals; despite high uncertainties, the most likely value for all crystals was close to that of the previously found orthorhombic polymorph of the anhydrous state ( $V \approx 1450 \text{ \AA}^3$ ), indicating dehydration of the crystals during warm-up in vacuum.

To compare the behavior of the vacuum-dehydrated trehalose to an initially anhydrous sample, we repeated a measurement at room temperature following the same protocol with commercially available anhydrous trehalose. Different from the case of dehydration inside the vacuum, we observed good diffraction for all screened crystals and could solve the structure for nine datasets like that shown in Figure 1f. Furthermore, those crystals belonged to the monoclinic polymorph, which, instead of dehydration, is obtained after crystallization at a temperature above the melting point of the dihydrate [44].

### 3.2. Dynamical Refinement Using *CrysAlis<sup>Pro</sup>* and *Jana2020*

As of now, most structures in 3D ED are solved and refined using tools developed for X-ray diffraction, which besides adjusted atomic scattering factors, do not attempt to account for the properties of electron radiation. Specifically, the high elastic-scattering cross-sections of electrons lead to multiple diffraction and mutual interference between all excited beams (dynamical diffraction). The widely used assumption in crystallographic software that Bragg spot intensities should be proportional to the squared amplitude of the corresponding structure factors (kinematical diffraction) does not hold in this case, which is, however, used by most crystallographic refinement software. Making use of the kinematical approximation still yields satisfactory results, as data collection off zone axes [1], mosaicity on the nano-scale [45], and inelastic scattering [46] mitigate dynamical effects [9]. However, the usefulness of using full dynamical computations for refinement has now been demonstrated for a range of samples and techniques [34,47–50]. Specific advantages, besides improved refinement figures of merit such as R-values, include improved visibility of hydrogen atoms and guest molecules in framework materials thanks to lower noise in the reconstructed potentials [48,50], improved assignment of atom species [50], and sensitivity to the absolute structure of crystals [49] through differences between symmetry-equivalent reflections arising from dynamical effects. Dynamical refinement has been implemented in the structure solution and refinement package *Jana2006*/*Jana2020* [35,36] for 3D ED data collected via the methods of precession tomography or, more recently, continuous rotation [50]. For the latter collection type, which is employed in the XtaLAB Synergy-ED diffractometer, unmerged intensities need to be computed for overlapping virtual frames (OVFs) at regular angular increments following the prescription of Klar et al. [50]. This currently can be performed using either the PETS2 processing software [51] or *CrysAlis<sup>Pro</sup>* version 43.22a or higher. Due to the complexity and many parameters of the processing pipelines, differences between the final intensities assigned to the diffraction spots in the OVFs are expected between the processing programs. As a benchmark case, we collected 3D ED data from a nanocrystal of the amino acid *L*-tyrosine. After kinematical refinement without hydrogens and isotropic displacement parameters, we obtain a solution with R-values  $R_1 = 14.4\%$  and  $wR_2 = 35.4\%$ . We next subjected this initial model

to further dynamical refinement in Jana2020 following the procedures as outlined in the literature [36,50]. In consecutive steps, we added (1) frame scaling and crystal thickness (with fixed atomic structure), (2) the atom positions and isotropic displacement parameters, (3) free hydrogen positions, and (4) anisotropic displacement parameters (ADPs) as refinement parameters. This procedure was repeated for data processed by CrysAlis<sup>Pro</sup> 43.49a and PETS2.2, respectively, with the initial model as *L*- and inverted *D*-enantiomer (equivalently referred to as *S*- and *R*-enantiomer). The resulting R-values are displayed in Figure 2b,c. Regardless of the input data and refinement type, we observe a clear preference for the correct chirality, and each of the refinement steps further decreases the R-values until they finally reach approximately half their values from kinematical refinement ( $R_1 = 7.6\%$ ,  $wR_2 = 22\%$  for CrysAlis<sup>Pro</sup> and *L*-configuration, Table S2), in accordance with typical behavior documented in the literature. There are minor quantitative differences between refinements against OVF intensities obtained from PETS2 and CrysAlis<sup>Pro</sup> (CAP); remarkably, while CrysAlis<sup>Pro</sup>-processed data refined to lower  $R_1$  values, the  $wR_2$  values are higher, which we attributed to differences in the error model corrections of the programs. Still, we find no major qualitative deviations. To obtain a more quantitative measure for the confidence level of absolute structure assignment, as originally suggested by Le Page et al. [52], we compute the background noise-adjusted z-score for the bias of observed intensities towards those computed from the correct absolute configuration following the definition of Klar et al. [50]. Z-scores higher than  $3\sigma$  were found for even the simplest computation, with values reaching up to  $10.0\sigma$  for data processing in CAP and full refinement in Jana2020, as shown in Figure 2d. Also, here, we find only minor deviations between the processing programs, likely arising from noise models and details of OVF computation.

Another representative example of absolute structure determination using CrysAlis<sup>Pro</sup> / Jana2020 for a larger chiral compound is the structure of the common antibiotic drug clarithromycin. A structure solution from a grain found to be of the solvent-free form II polymorph [53,54] is shown in Figure 2e, which after kinematical refinement in SHELXL resulting in  $R_1 = 14.8\%/wR_2 = 31.9\%$ , was subjected to dynamical refinement in Jana2020 with crystal thickness (EDthick), atom positions, and isotropic displacement parameters as free parameters, leading to a large gap between the correct ( $R_1 = 13.0\%/wR_2 = 25.7\%$ , Table S3) and incorrect ( $R_1 = 16.7\%/wR_2 = 31.3\%$ ) absolute configuration with an adjusted z-score of 14.0.

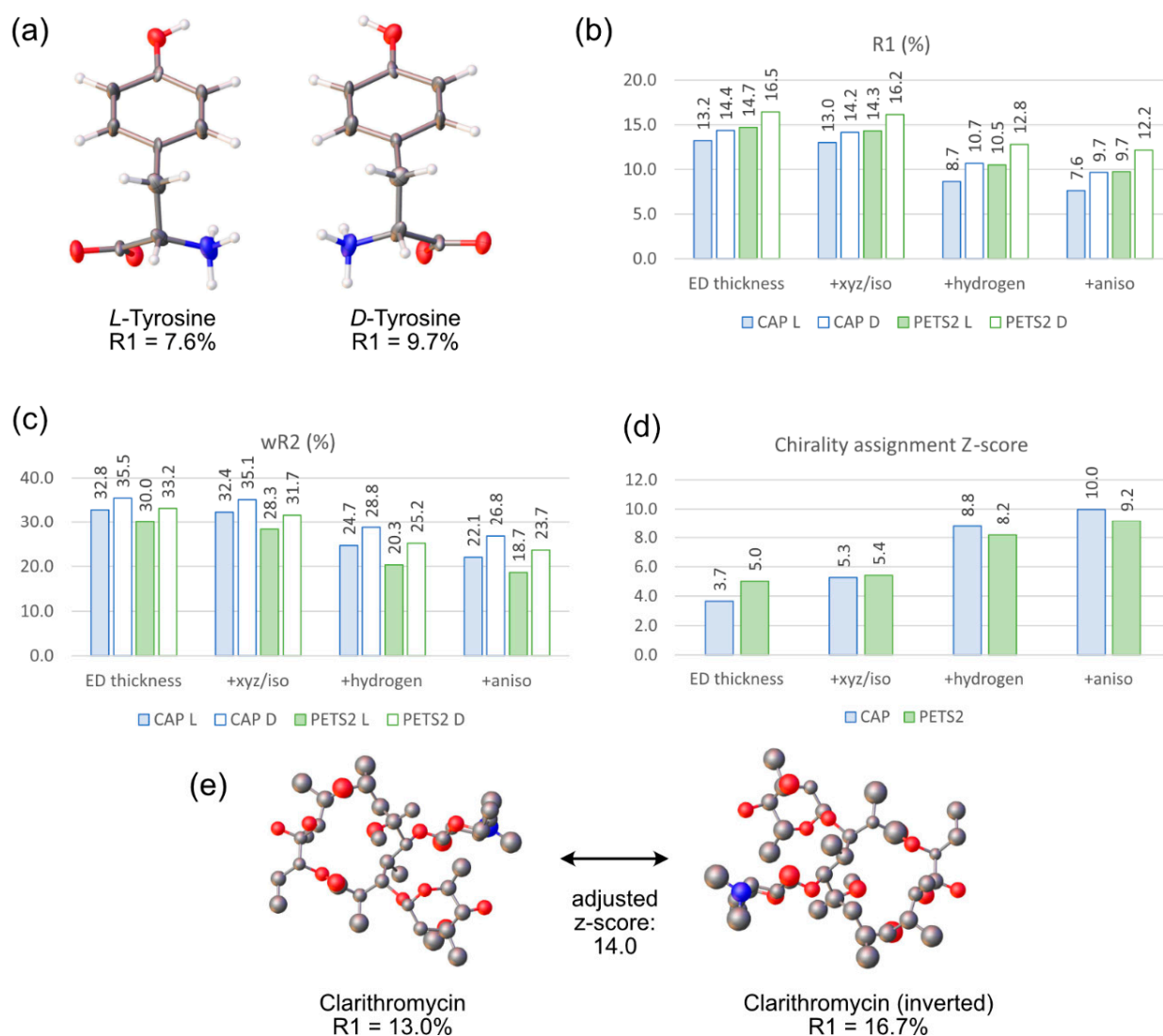


**Figure 2.** Dynamical refinement of crystal structures from *L*-tyrosine and clarithromycin. (a) Drawings of the tyrosine structure solved as *L*- and *D*-enantiomer with resulting  $R_1$  values after dynamical refinement. (b)  $R_1$  values after dynamical refinement of tyrosine crystal structures processed with CrysAlis<sup>Pro</sup> (CAP, blue) and PETS2 (green) for *L*- (filled) and *D*- (empty) enantiomers after several types of refinements applied. (c) As (b), with  $wR_2$  as figure of merit. (d) Z-score (background-noise-adjusted) for correct determination of enantiomer by comparing observed intensities to predictions from refinements with both *L*- and *D*-configuration. (e) Correct and inverted configuration of clarithromycin after dynamical refinement with respective  $R_1$  value.

### 3.3. Operation at Large Crystal-to-Detector Distances for Proteins and Small Molecules

All TEMs (except for some dedicated STEMs) allow one to set the magnification of the projection of images onto the detector by means of changing currents in the electron lenses below the sample. If set to diffraction mode, this corresponds to changing the effective crystal-to-detector distance (DD), equivalent to changing the physical detector position along the beam direction on an X-ray diffractometer. Featuring a similar projection system, the XtaLAB Synergy-ED diffractometers used in this study allow one to choose between calibrated DD settings ranging between approximately 500 mm and 2500 mm, providing the ability to both collect data at high resolutions up to  $\approx 0.3$  Å, as well as resolve closely spaced reflections arising from the large unit cells of, among others, protein crystals or mesoporous compounds.

For the former scenario, the question arises of what minimum DD and hence peak spacing on the newly introduced detector is required for a typical protein crystal when using the combination of the HyPix-ED detector and processing in CrysAlis<sup>Pro</sup>. We collected a dataset from a focused ion beam milled lamella of a thaumatin microcrystal (Figure 3a,b) with a tetragonal unit cell ( $a = b = 58.4 \text{ \AA}$ ,  $c = 151.2 \text{ \AA}$ ), which is a commonly used standard for 3D ED on proteins [55,56]. DD was set to 1800 mm, potentially keeping spots out to  $\sim 1.2 \text{ \AA}$  (resolution at detector edge) covered by the detector. In Figure 3c,d, we show frames from the dataset viewed perpendicular to the  $c$ -axis with a Bragg spot spacing of 0.30 mm (3 pixels) on the detector. Despite this small spacing, the data could be integrated by CrysAlis<sup>Pro</sup> using default two-pass profile fitting and were further processed using a standard molecular-replacement pipeline to a final protein structure at a resolution of 2.15  $\text{\AA}$  (Figure 3e, see Table S4 and Section 2.3 for details).

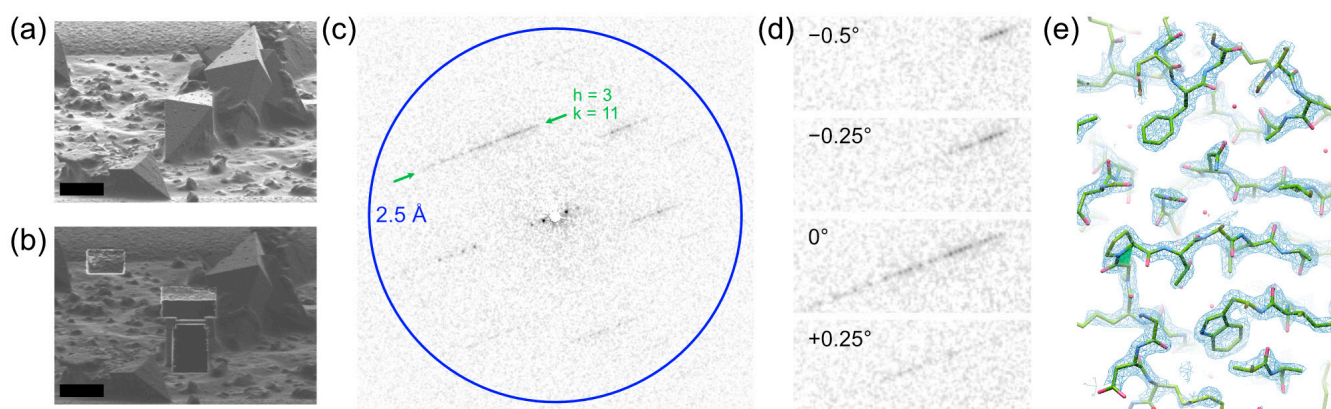


**Figure 3.** Three-dimensional ED data collection from a protein microcrystal. (a,b) SEM images of thaumatin crystals on a vitrified TEM grid imaged before (a) and after (b) FIB milling. Scale bars correspond to 10  $\mu\text{m}$ . The thin lamella section in (b) is used for data collection. (c) Diffraction frame from continuous rotation collection over a wedge of  $0.25^\circ$  nearly perpendicular to the tetragonal  $c$ -axis. The indicated streak corresponds to reflections with  $h = 3$ ,  $k = 11$ . (d) Close-ups of the indicated streak from the frame shown in (c) and adjacent frames spaced by  $0.25^\circ$ . (e) Section from structure solution with  $2F_{\text{obs}} - F_{\text{calc}}$  at  $2\sigma$ .

While the advantages of using a short DD for small-molecule crystallography, in particular on inorganic compounds with small unit cells and diffracting to high resolutions, are obvious, the case for longer DD is more subtle. For a challenging test sample exhibiting an unusually long unit cell axis as well as a tendency for twinning and a poor overall diffraction signal, we used cystine, an oxidized amino acid forming a hexagonal polymorph with a  $c$ -axis of  $\approx 58 \text{ \AA}$  length. Both at 100 K and 293 K, we found most crystal grains to be very poorly diffracting or badly twinned. Using automated screening collection (unattended queue mode,  $4^\circ$  collection range) from approximately 100 manually selected candidate crystals on two grids, we identified two well-diffracting, only weakly intergrown crystals at starkly different orientations with respect to the sample grid (Figure 4a–f). While crystal 1 exhibited a plate-like morphology and was oriented with its long  $c$ -axis almost perpendicular to the grid (Figure 4a–c), crystal 2 had its  $c$ -axis almost in the plane of the sample grid (Figure 4d–f). For each of the crystals, we conducted three data collections at an identical crystal orientation and scan range but different settings of DD. We also used a fine frame slicing/scan width of  $0.15^\circ$  for optimal resolution of peaks in three dimensions, which, due to the noise-free readout of the hybrid-pixel detector, does not impact signal-to-noise ratios.

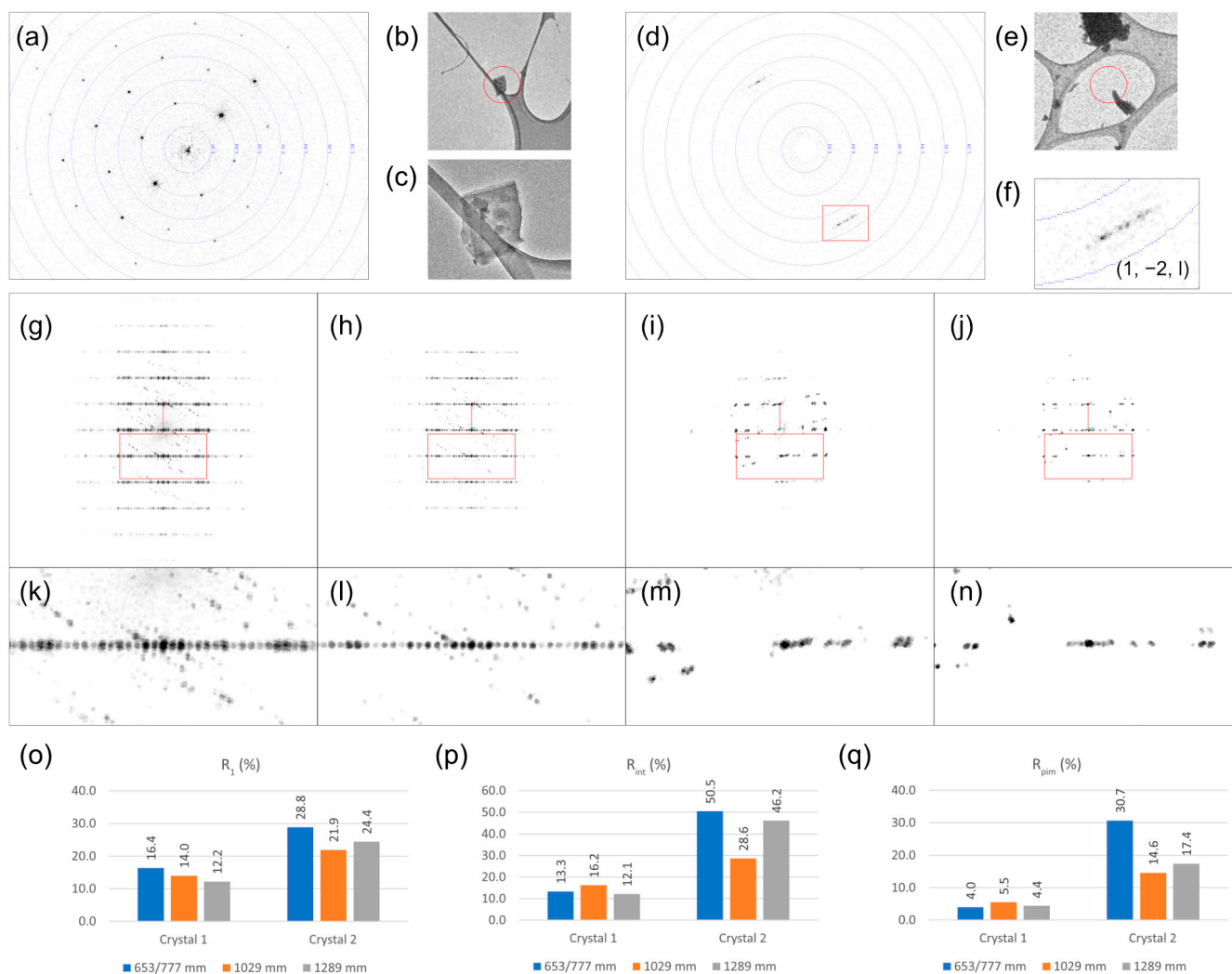


**Figure 4.** Diffraction data collection from two grains of hexagonal cystine. (a) Diffraction pattern near neutral tilt at DD = 1289 mm, (b) real-space image, (c) close-up image for crystal 1. The red circle in (b) corresponds to the region that diffraction was collected from using a selected-area aperture of apparent diameter 2  $\mu\text{m}$ . (d) Diffraction pattern near neutral tilt at DD = 1289 mm, with red box indicating zoom region in (f), (e) real-space image, (f) zoom into diffraction pattern for crystal 2. (g) 3D reconstruction of reciprocal space from pixel intensities, projected along  $b^*$  for crystal 1 at DD = 653 mm. The shown region corresponds to  $(0.8 \text{ \AA})^{-1}$  along each axis. The red box indicates the zoom region shown in (k). (h) Same, at DD = 1289 mm. (i) Same, for crystal 2 at DD = 777 mm. (j) Same, for crystal 2 at DD = 1289 mm. (k–n) Zoomed sections of (g–j), respectively, highlighting reflections with  $h = 1$ . (o)  $R_1$  values after refinement in SHELXL, for three DD values for each crystal. (p)  $R_{int}$  values after integration, scaling, and merging in CrysAlis<sup>Pro</sup>. (q)  $R_{pim}$  values.

Overall, crystal 1 yielded significantly better data, as expected, due to the absence of strong peak overlaps with the  $c^*$ -axis never passing the (almost flat) Ewald sphere within the collected wedge of  $125^\circ$ . Additionally, the thin plate-like morphology minimizes the detrimental effects of inelastic scattering by diffusing the spots and dynamical diffraction. In Figure 4g,h, projections of reciprocal space reconstructed from pixel intensities in the collected frames are shown along the  $b^*$ -axis for the shortest and longest DD. While peaks are well-separated and aligned in an undistorted lattice along all axes, the long DD yields better-defined spots along the  $a^*$ -direction, as seen in the close-up views of peaks with  $h = 1$  in Figure 4k,l. This comes at the expense of a more pronounced cut-off at higher resolution due to more limited detector coverage. Despite the unproblematic geometry, we observed the best refinement metric  $R_1$  from the longest DD of 1289 mm (Figure 4o,

Table S5) at similar precision indicators  $R_{\text{int}}$  and  $R_{\text{pim}}$  (Figure 4p,q). This suggests that the higher data redundancy achieved at low DD is outweighed by higher accuracy of integrated intensities due to better peak fitting and decreased overlap, specifically with a weak intergrown second crystal.

The case of crystal 2 is significantly more challenging, as frames collected almost normal to the grid exhibit tightly spaced and more diffuse peaks (Figure 4d,f). The latter is due to the crystal, despite its small size, retaining a plate-like geometry and hence a greater thickness perpendicular to the  $c$ -axis. As can be seen in Figure 4i,j,m,n, besides a lower resolution (cut at 1.1 Å for processing), the reconstructed reciprocal space shows poorly separated peaks as well as spatial distortions, specifically at the lowest DD. This was chosen as 777 mm instead of 653 mm, as for crystal 1, to avoid peak spacing along  $c^*$  falling below 0.3 mm. We attribute this to a poor determination of crystal orientation. Both issues are mitigated by longer DD settings, significantly improving the quality of processing and refinement (Figure 4o–q, Table S5). Optimal quality is reached at the intermediate distance, which we hypothesize to be related to spurious factors such as the onset of radiation damage or crystal drift in the longest-DD dataset.

#### 4. Discussion

With the advent of commercially available, fully integrated diffractometers [10,11], 3D ED is transitioning from an exploratory new approach developed within a dedicated method-centered community to a cutting-edge technique offered by an increasing number of crystallographic facilities. As such, it is becoming available to a wide audience of non-specialist users from diverse fields who might not yet be familiar with practicalities that differ from common knowledge in X-ray crystallography. In this work, we conducted systematic measurements on test systems, specifically targeting three such aspects to be considered for a successful 3D ED experiment. We will further discuss the outcomes of those in the following.

##### 4.1. Cryo-Transfer Allows Data Collection from Hydrates and Solvates

The ability to protect samples from dehydration in the diffractometer vacuum is critical for a wide range of substances, such as hydrates, solvates, and biomolecules. While the creation of atmospheric micro-environments [57–59] using specific sample holders is possible, cryo-transfer, where the sample grid is cooled to low temperature outside the vacuum and transferred into the vacuum in a cold state, is a significantly simpler, faster, and cheaper workflow. While cryo-transfer is now commonplace in cryo-electron microscopy or 3D-ED/MicroED on biomolecules [7,60], its strict necessity for many small molecule samples is less appreciated.

Our findings on dehydration of trehalose dihydrate (and prevention thereof) in Section 3.1 are entirely consistent with the hypothesis of complete preservation of crystallites using cryo-transfer. Insertion into a vacuum without cryo-protection or warm-up after cryo-transfer not only leads to dehydration, but in most cases, also partial or complete loss of crystallinity. As a corollary, this means that there may be cases where it is not possible to distinguish between a sample that has collapsed due to being unprotected in a vacuum and one that exhibits poor crystallinity from the start. This underlines the necessity of additional PXRD measurements, ideally during or after exposure to vacuum, if no cryo-transfer is possible. Furthermore, we could show that in-vacuum cooling of the small fraction of crystals that dehydrated without collapse of the crystal lattice only leads to a marginal improvement in data quality. It was recently reported by Yang et al. [61] that cryogenic data collection even decreased data quality for test systems, including an anhydrous sugar, highlighting that the impact of temperature for vacuum-insensitive samples is highly sample-dependent and warrants further study. Of note, dehydrated crystals were of the rare orthorhombic polymorph [42], which differs in its unit cell parameters from the dihydrate by a small but well-detectable margin, whereas commercially obtained

anhydrous crystals were also measured and found to be well-diffracting and of the more common monoclinic polymorph [44].

While trehalose dihydrate is only one specific example of a hydrated microcrystalline compound, the observed behaviors are commonly found in our laboratories for a wide range of small molecule samples, specifically pharmaceuticals and solvated mesoporous compounds, which are regularly solved on request by commercial and academical customers and collaborators.

#### 4.2. Absolute Structure Determination Using a Simplified Workflow

Among the virtues of dynamical diffraction effects in electron diffraction, the determination of absolute structure and, thus, the chirality of the studied compound [49,50] is particularly outstanding for the field of pharmaceuticals and for organic small molecules, among others. The necessary intensity differences between Bijvoet-pairs, however, arise from a fundamentally different physical mechanism than that of resonance scattering of X-rays and cannot be accounted for within the kinematical approximation, such that only dynamical refinement strategies based on Bloch-wave or multi-slice computations [35,62–64] are able to make use of the chiral information contained in 3D ED data.

Inevitably, routine application of dynamical refinement for absolute structure determination poses new challenges both in terms of knowledge and practical skills of crystallographers, as well as the required computation time of the order of hours for a full dynamical refinement, even on high-end workstations. While progress in available packages [36] will help to somewhat lower those barriers, the necessary workflows are still significantly more intricate than what typical users of highly integrated X-ray diffractometers are used to.

As we have shown by a benchmarking series on a standard sample in Section 3.2, data processing using the latest versions of CrysAlis<sup>Pro</sup> provides data suitable for dynamical refinement (OVF intensities). The data output leads to results comparable to that achieved by reprocessing in PETS2 [51] when used for dynamical refinement in Jana2020 [36,65]. OVF intensities are computed automatically during data collection on an XtaLAB Synergy-ED diffractometer, such that, along with a starting model provided by AutoChem/Olex2 [28], a full set of input files for dynamical refinement is available immediately after data collection. This significantly speeds up the workflow for dynamical refinement. Furthermore, we showed that even without the refinement of atomic coordinates and ADPs, comparison to dynamically predicted intensities after frame scaling and crystal thickness refinement [65] gives a satisfactory degree of confidence for absolute structure determination, as gauged by z-scores well exceeding  $3\sigma$ , and differences in R-values shown in Figure 2. For determination of absolute structure with the highest fidelity, as well as full exploitation of the information contained in 3D ED data from both organic and inorganic compounds, such as high visibility of hydrogens and guest molecules, more accurate bond lengths, and more confident assignment of atom species [50], a full refinement (presented in detail elsewhere [50,65]) is inevitably required; however, for proper absolute structure determination, a single round of dynamical parameter optimization in Jana2020 following CrysAlis<sup>Pro</sup> data reduction can give a good indication of absolute structure within a few minutes after data collection. Very recently, the absolute structures of the active pharmaceutical ingredient levocetirizine dihydrochloride and the natural product hakuhybotrol were determined using similar workflows [16,20].

#### 4.3. Appropriate Detector Distance Can Improve Data Quality

TEMs, as well as the XtaLAB Synergy-ED diffractometer, allow setting the detector distance prior to measurement by merely changing a preset in the control software, leading to questions on how to pick an optimal detector distance (DD) for a given sample. For protein crystals, long DDs are clearly required at the expense of high-resolution coverage, which scales reciprocally with the accessible unit cell length. As a rule of thumb, the DD should be larger than  $(p\Delta N) \cdot c / \lambda$ , where  $p$ ,  $c$ ,  $\lambda$  denote pixel size, longest unit cell axis, and wavelength, respectively. The factor  $\Delta N$ , representing the number of pixels that peaks

should be separated by, depends on the point-spread function of the detector, as well as the performance of the used integration algorithm. The successful data processing of a thaumatin protein crystal collected at a DD set to an aggressively low value of  $\approx 1800$  mm indicates that  $\Delta N \approx 3$  is sufficient for the combination of the HyPix-ED detector with CrysAlis<sup>Pro</sup>. We attribute this to the relatively large pixel size of  $100 \mu\text{m}$  leading to a narrow point spread even with 200 keV electrons [66] and the sophisticated multi-pass profile fitting protocols in CrysAlis<sup>Pro</sup>. This finding implies that a maximum unit cell length of more than  $200 \text{ \AA}$  is still compatible with standard settings on the XtaLAB Synergy-ED, even while retaining detector coverage up to  $1.7 \text{ \AA}$  at near the far edge of the detector.

Besides the case of protein crystals, small-molecule 3D ED can also profit from longer DD settings, as we have demonstrated by the example of cystine nanocrystals, combining an exceptionally long unit cell axis, a tendency for intergrowth and twinning, and a high symmetry. For the case of a crystal showing relatively low-resolution diffraction and with a large portion of the collected data having close peak spacing on each frame due to the flat Ewald sphere lying close to a long axis and diffuse inelastic scattering, common settings of DD for small-molecule work were unable to yield satisfactory data quality. It is evident that increasing DD in this scenario leads to a significant improvement. More surprisingly, long DD settings otherwise associated with protein crystals even slightly improved data quality in an unproblematic crystal where no close peak spacing on single frames was observed, but the reduced data redundancy at high resolutions might have been outweighed by decreased residual peak overlap for rejection of a small intergrown crystal, and higher accuracy of crystal orientation and peak fitting. It should be noted that this trade-off might be more unfavorable in the case of lower symmetry, where low completeness at high resolutions due to angular coverage becomes a limiting factor. Also, while our measurements have been conducted on a counting detector with no background noise, an instrument fitted with a conventional CMOS or CCD detector might yield worse signal-to-noise ratios at larger DD as more background noise is collected from the larger integration regions required to fit the magnified peaks. Still, those findings indicate that, for data collection of compounds with unknown properties with regards to diffraction resolution, propensity for intergrowth and twinning, as well as diffuse inelastic scattering, the choice of a larger DD than usual should be taken into consideration, despite a possible penalty in completeness or precision (though not accuracy) of reflection intensities. This might be especially useful for upcoming applications in high-throughput, automated screening of heterogeneous mixtures [67–70], which will frequently contain such sub-optimal crystals that nevertheless need to be included in data analysis as effectively as possible. At the other end of the spectrum, inorganic compounds will often yield useful diffraction up to very high resolutions; in this case, further shortening the DD below typical values will lead to improved resolution and completeness, which would be useful, e.g., for charge-density studies or dynamical refinement.

## 5. Conclusions and Outlook

In this paper, we conducted measurements on representative samples, addressing three particular aspects of experiment design for 3D ED/MicroED, that is, preservation of hydration by cryo-transfer, simple dynamical refinement for determination of absolute structure, and optimal choice of effective crystal-to-detector distance. All those are of immediate interest for practical work on TEMs and electron diffractometers, using workflows and instrumentation available in dedicated research groups and, increasingly, general crystallographic facilities.

Along with the adoption of 3D ED/MicroED into the canon of structure determination methods, new approaches regarding sample preparation, data collection, data processing, and structure solution are rapidly developing, such as high-throughput crystallinity screening [67], on-grid crystallization [71], lipid cubic phase embedded crystals [72], environmental cells [57,58,73], efficient analysis of heterogeneous samples [68–70], autonomous and serial data collection [69,74–76], low-resolution phasing [77], dynamical refinement [47,48,64],

absolute structure determination [49,50], diffuse scattering and pair-distribution functions [78,79], and aspherical atom models [80], among many others. Assessing the new opportunities provided by such exciting developments in everyday work and casting them into dependable workflows will be an important task for years to come. Hence, while our current study is limited to relatively basic parameters, we are hoping for many more investigations on deriving best practices for obtaining the best structures possible, from a broad array of sample types, while minimizing the effort for individual optimization for each sample.

**Supplementary Materials:** The following supporting information can be downloaded at: <https://www.mdpi.com/article/10.3390/sym15081555/s1>, Table S1: Trehalose; Table S2: Tyrosine; Table S3: Clarithromycin; Table S4: Thaumatin; Table S5: Cystine.

**Author Contributions:** Sample preparation and data collection were performed by K.-N.T., S.I., J.M.W., C.R.G., C.J.S., A.Y., E.O., Y.A., T.M., N.H. and R.B. Data processing and structure solution were performed by K.-N.T., S.I., M.D.C., J.B.-B., E.C.E.-A. and R.B. Crystallographic data files were prepared by K.-N.T., M.D.C. and R.B. The project was conceived and super-vised by A.Y., F.J.W., J.D.F. and R.B. The manuscript was written by R.B. with contributions from all authors. All authors have read and agreed to the published version of the manuscript.

**Funding:** This research received no external funding.

**Data Availability Statement:** Several molecular structures from this work are deposited in the Cambridge Structural Database (CSD) or, respectively, the Protein Database (PDB), using accession codes as quoted in the crystallographic data tables. Ancillary molecular structures solved solely for the purpose of systematic comparisons are available upon request from the authors.

**Acknowledgments:** We are grateful to Hiroyasu Sato, Takashi Kikuchi, and Keigo Takahira for assistance with experiment data management. We appreciate helpful discussions on data processing with Mathias Meyer Michał Jasnowski and Przemysław Stec.

**Conflicts of Interest:** All authors except for J.B.-B. and E.C.E.-A. are current or former employees of subsidiaries of the Rigaku Holdings Corporation or JEOL Limited, which are partners in the development of the XtaLAB Synergy-ED diffractometer. They have no conflicting interests, financial or otherwise, and declare that their affiliation with either company had no influence on the design or interpretation of the experiments.

## References

1. Kolb, U.; Gorelik, T.; Kübel, C.; Otten, M.T.; Hubert, D. Towards Automated Diffraction Tomography: Part I-Data Acquisition. *Ultramicroscopy* **2007**, *107*, 507–513. [[CrossRef](#)] [[PubMed](#)]
2. Mugnaioli, E.; Gorelik, T.; Kolb, U. “Ab Initio” Structure Solution from Electron Diffraction Data Obtained by a Combination of Automated Diffraction Tomography and Precession Technique. *Ultramicroscopy* **2009**, *109*, 758–765. [[CrossRef](#)] [[PubMed](#)]
3. Zhang, D.; Oleynikov, P.; Hovmöller, S.; Zou, X. Collecting 3D Electron Diffraction Data by the Rotation Method. *Z. Krist.* **2010**, *225*, 94–102. [[CrossRef](#)]
4. Nederlof, I.; van Genderen, E.; Li, Y.-W.; Abrahams, J.P. A Medipix Quantum Area Detector Allows Rotation Electron Diffraction Data Collection from Submicrometre Three-Dimensional Protein Crystals. *Acta Crystallogr. D Biol. Crystallogr.* **2013**, *69*, 1223–1230. [[CrossRef](#)]
5. Shi, D.; Nannenga, B.L.; Iadanza, M.G.; Gonen, T. Three-Dimensional Electron Crystallography of Protein Microcrystals. *eLife* **2013**, *2*, e01345. [[CrossRef](#)]
6. Gemmi, M.; Mugnaioli, E.; Gorelik, T.E.; Kolb, U.; Palatinus, L.; Boullay, P.; Hovmöller, S.; Abrahams, J.P. 3D Electron Diffraction: The Nanocrystallography Revolution. *ACS Cent. Sci.* **2019**, *5*, 1315–1329. [[CrossRef](#)]
7. Nannenga, B.L.; Gonen, T. The Cryo-EM Method Microcrystal Electron Diffraction (MicroED). *Nat. Methods* **2019**, *16*, 369–379. [[CrossRef](#)]
8. Gruene, T.; Holstein, J.J.; Clever, G.H.; Keppler, B. Establishing Electron Diffraction in Chemical Crystallography. *Nat. Rev. Chem.* **2021**, *5*, 660–668. [[CrossRef](#)]
9. Saha, A.; Nia, S.S.; Rodríguez, J.A. Electron Diffraction of 3D Molecular Crystals. *Chem. Rev.* **2022**, *122*, 13883–13914. [[CrossRef](#)]
10. Ito, S.; White, F.J.; Okunishi, E.; Aoyama, Y.; Yamano, A.; Sato, H.; Ferrara, J.D.; Jasnowski, M.; Meyer, M. Structure Determination of Small Molecule Compounds by an Electron Diffractometer for 3D ED/MicroED. *CrystEngComm* **2021**, *23*, 8622–8630. [[CrossRef](#)]
11. Simoncic, P.; Romeijn, E.; Hovestreydt, E.; Steinfeld, G.; Santiso-Quiñones, G.; Merkelbach, J. Electron Crystallography and Dedicated Electron-Diffraction Instrumentation. *Acta Crystallogr. Sect. E Crystallogr. Commun.* **2023**, *79*, 410–422. [[CrossRef](#)] [[PubMed](#)]

12. Kahlenberg, V.; Vinke, J.; Krüger, H.; Ito, S.; Schürmann, C.J.  $\text{Na}_2\text{Ca}_3\text{Si}_2\text{O}_8$  or  $\gamma\text{-Na}_2\text{Ca}_6\text{Si}_4\text{O}_{15}$ ? A Hybrid Approach Combining 3D Single-Crystal Electron and Powder X-Ray Diffraction. *J. Am. Ceram. Soc.* **2022**, *105*, 6976–6998. [[CrossRef](#)]
13. Pearce, N.; Reynolds, K.E.A.; Kayal, S.; Sun, X.Z.; Davies, E.S.; Malagrecia, F.; Schürmann, C.J.; Ito, S.; Yamano, A.; Argent, S.P.; et al. Selective Photoinduced Charge Separation in Perylene-3,4,9,10-tetracarboxylic Diimide-Pillar[5]Arene Rotaxanes. *Nat. Commun.* **2022**, *13*, 415. [[CrossRef](#)] [[PubMed](#)]
14. Steinke, F.; Otto, T.; Ito, S.; Wöhlbrandt, S.; Stock, N. Isostructural Family of Rare-Earth MOFs Synthesized from 1,1,2,2-Tetrakis(4-Phosphonophenyl)Ethylene. *Eur. J. Inorg. Chem.* **2022**, *2022*, e202200562. [[CrossRef](#)]
15. Jandl, C.; Steinfeld, G.; Li, K.; Pang, P.K.C.; Choi, C.L.; Wang, C.; Simoncic, P.; Williams, I.D. Absolute Structure Determination of Chiral Zinc Tartrate MOFs by 3D Electron Diffraction. *Symmetry* **2023**, *15*, 983. [[CrossRef](#)]
16. Karothu, D.P.; Alhaddad, Z.; Göb, C.R.; Schürmann, C.J.; Bücker, R.; Naumov, P. The Elusive Structure of Levocetirizine Dihydrochloride Determined by Electron Diffraction. *Angew. Chem. Int. Ed.* **2023**, *62*, e202303761. [[CrossRef](#)]
17. Mies, T.; Schürmann, C.; Ito, S.; White, A.J.P.; Crimmin, M.R.; Barrett, A.G.M. Synthesis and Characterization of a Calcium-Pyrazolonato Complex. Observation of In-Situ Desolvation during Micro-Electron Diffraction. *Z. Anorg. Allg. Chem.* **2023**, *649*, e202200294. [[CrossRef](#)]
18. Perera, T.A.; Taylor, W.V.; Gildner, M.B.; Reinheimer, E.W.; Ito, S.; Nelson, A.; Yost, S.R.; Hudnall, T.W. Photochemical Reactions of a Diamidocarbene: Cyclopropanation of Bromonaphthalene, Addition to Pyridine, and Activation of  $\text{Sp}^3$  C–H Bonds. *Chem. Sci.* **2023**, *14*, 7867–7874. [[CrossRef](#)]
19. Shivanna, M.; Zheng, J.-J.; Ray, K.G.; Ito, S.; Ashitani, H.; Kubota, Y.; Kawaguchi, S.; Stavila, V.; Yao, M.-S.; Fujikawa, T.; et al. Selective Sorption of Oxygen and Nitrous Oxide by an Electron Donor-Incorporated Flexible Coordination Network. *Commun. Chem.* **2023**, *6*, 62. [[CrossRef](#)]
20. Watanabe, Y.; Takahashi, S.; Ito, S.; Tokiwa, T.; Noguchi, Y.; Azami, H.; Kojima, H.; Higo, M.; Ban, S.; Nagai, K.; et al. Hakuhybotrol, a Polyketide Produced by *Hypomyces Pseudocorticicola*, Characterized with the Assistance of 3D ED/MicroED. *Org. Biomol. Chem.* **2023**, *21*, 2320. [[CrossRef](#)]
21. Xue, Z.; Zheng, J.-J.; Nishiyama, Y.; Yao, M.-S.; Aoyama, Y.; Fan, Z.; Wang, P.; Kajiwara, T.; Kubota, Y.; Horike, S.; et al. Fine Pore-Structure Engineering by Ligand Conformational Control of Naphthalene Diimide-Based Semiconducting Porous Coordination Polymers for Efficient Chemiresistive Gas Sensing. *Angew. Chem. Int. Ed.* **2023**, *62*, e202215234. [[CrossRef](#)]
22. Andersen, C.E.; McPherson, J.N.; Giménez-Marqués, M.; Li, J.; Kubus, M.; Ito, S.; Goeb, C.R.; Ott, S.; Larsen, R.W.; Espallargas, G.M.; et al. Vapor-Phase Synthesis of Low-Valent Metal-Organic Frameworks from Metal Carbonyl Synthons. *J. Mater. Chem. C* **2023**. [[CrossRef](#)]
23. Kubens, L.; Truong, K.-N.; Lehmann, C.W.; Lützenkirchen-Hecht, D.; Bornhorst, J.; Mohr, F. The structure of Maneb: An important manganese-containing bis(dithiocarbamate) fungicide. *Chem. Eur. J.* **2023**, e202301721. [[CrossRef](#)] [[PubMed](#)]
24. *Rigaku Oxford Diffraction CrysAlisPro Software System*; Rigaku Corporation: Wrocław, Poland, 2023.
25. Duyvesteyn, H.M.E.; Kotecha, A.; Ginn, H.M.; Hecksel, C.W.; Beale, E.V.; de Haas, F.; Evans, G.; Zhang, P.; Chiu, W.; Stuart, D.I. Machining Protein Microcrystals for Structure Determination by Electron Diffraction. *Proc. Natl. Acad. Sci. USA* **2018**, *115*, 9569–9573. [[CrossRef](#)] [[PubMed](#)]
26. Peet, M.J.; Henderson, R.; Russo, C.J. The Energy Dependence of Contrast and Damage in Electron Cryomicroscopy of Biological Molecules. *Ultramicroscopy* **2019**, *203*, 125–131. [[CrossRef](#)]
27. Martynowycz, M.W.; Clabbers, M.T.B.; Unge, J.; Hattne, J.; Gonen, T. Benchmarking the Ideal Sample Thickness in Cryo-EM. *Proc. Natl. Acad. Sci. USA* **2021**, *118*, e2108884118. [[CrossRef](#)]
28. *Rigaku Oxford Diffraction AutoChem in Conjunction with Olex2*; Rigaku Corporation: Wrocław, Poland, 2023.
29. Cichocka, M.O.; Ångström, J.; Wang, B.; Zou, X.; Smeets, S. High-Throughput Continuous Rotation Electron Diffraction Data Acquisition via Software Automation. *J. Appl. Crystallogr.* **2018**, *51*, 1652–1661. [[CrossRef](#)]
30. de la Cruz, M.J.; Martynowycz, M.W.; Hattne, J.; Gonen, T. MicroED Data Collection with SerialEM. *Ultramicroscopy* **2019**, *201*, 77–80. [[CrossRef](#)]
31. Cheng, A.; Negro, C.; Bruhn, J.F.; Rice, W.J.; Dallakyan, S.; Eng, E.T.; Waterman, D.G.; Potter, C.S.; Carragher, B. Leginon: New Features and Applications. *Protein Sci.* **2021**, *30*, 136–150. [[CrossRef](#)]
32. Sheldrick, G.M. SHELXT—Integrated Space-Group and Crystal-Structure Determination. *Acta Crystallogr. Sect. Found. Adv.* **2015**, *71*, 3–8. [[CrossRef](#)]
33. Sheldrick, G.M. A Short History of SHELX. *Acta Crystallogr. A* **2008**, *64*, 112–122. [[CrossRef](#)] [[PubMed](#)]
34. Yang, T.; Xu, H.; Zou, X. Improving Data Quality for Three-Dimensional Electron Diffraction by a Post-Column Energy Filter and a New Crystal Tracking Method. *J. Appl. Crystallogr.* **2022**, *55*, 1583–1591. [[CrossRef](#)]
35. Palatinus, L.; Petříček, V.; Corrêa, C.A. Structure Refinement Using Precession Electron Diffraction Tomography and Dynamical Diffraction: Theory and Implementation. *Acta Crystallogr. Sect. Found. Adv.* **2015**, *71*, 235–244. [[CrossRef](#)] [[PubMed](#)]
36. Petříček, V.; Palatinus, L.; Plášil, J.; Dušek, M. JANA2020—A New Version of the Crystallographic Computing System Jana. *Z. Krist. Cryst. Mater.* **2023**. [[CrossRef](#)]
37. Evans, P.R.; Murshudov, G.N. How Good Are My Data and What Is the Resolution? *Acta Crystallogr. D Biol. Crystallogr.* **2013**, *69*, 1204–1214. [[CrossRef](#)] [[PubMed](#)]
38. McCoy, A.J.; Grosse-Kunstleve, R.W.; Adams, P.D.; Winn, M.D.; Storoni, L.C.; Read, R.J. Phaser Crystallographic Software. *J. Appl. Crystallogr.* **2007**, *40*, 658–674. [[CrossRef](#)]
39. Emsley, P.; Lohkamp, B.; Scott, W.G.; Cowtan, K. Features and Development of Coot. *Acta Crystallogr. D Biol. Crystallogr.* **2010**, *66*, 486–501. [[CrossRef](#)]

40. Murshudov, G.N.; Skubák, P.; Lebedev, A.A.; Pannu, N.S.; Steiner, R.A.; Nicholls, R.A.; Winn, M.D.; Long, F.; Vagin, A.A. REFMAC5 for the Refinement of Macromolecular Crystal Structures. *Acta Crystallogr. D Biol. Crystallogr.* **2011**, *67*, 355–367. [[CrossRef](#)]
41. Denysenko, D.; Grzywa, M.; Tonigold, M.; Streppel, B.; Krkljus, I.; Hirscher, M.; Mugnaioli, E.; Kolb, U.; Hanss, J.; Volkmer, D. Elucidating Gating Effects for Hydrogen Sorption in MFU-4-Type Triazolate-Based Metal-Organic Frameworks Featuring Different Pore Sizes. *Chem. Eur. J.* **2011**, *17*, 1837–1848. [[CrossRef](#)]
42. Nagase, H.; Ogawa, N.; Endo, T.; Shiro, M.; Ueda, H.; Sakurai, M. Crystal Structure of an Anhydrous Form of Trehalose: Structure of Water Channels of Trehalose Polymorphism. *J. Phys. Chem. B* **2008**, *112*, 9105–9111. [[CrossRef](#)]
43. Brown, G.M.; Rohrer, D.C.; Berking, B.; Beevers, C.A.; Gould, R.O.; Simpson, R. The Crystal Structure of  $\alpha,\alpha$ -Trehalose Dihydrate from Three Independent X-Ray Determinations. *Acta Crystallogr. B* **1972**, *28*, 3145–3158. [[CrossRef](#)]
44. Jeffrey, G.A.; Nanni, R. The Crystal Structure of Anhydrous  $\alpha,\alpha$ -Trehalose at  $-150^\circ$ . *Carbohydr. Res.* **1985**, *137*, 21–30. [[CrossRef](#)] [[PubMed](#)]
45. Gallagher-Jones, M.; Ophus, C.; Bustillo, K.C.; Boyer, D.R.; Panova, O.; Glynn, C.; Zee, C.; Ciston, J.; Mancina, K.C.; Minor, A.M.; et al. Nanoscale Mosaicity Revealed in Peptide Microcrystals by Scanning Electron Nanodiffraction. *Commun. Biol.* **2019**, *2*, 26. [[CrossRef](#)] [[PubMed](#)]
46. Latychevskaia, T.; Abrahams, J.P. Inelastic Scattering and Solvent Scattering Reduce Dynamical Diffraction in Biological Crystals. *Acta Crystallogr. Sect. B Struct. Sci. Cryst. Eng. Mater.* **2019**, *75*, 523–531. [[CrossRef](#)] [[PubMed](#)]
47. Palatinus, L.; Corrêa, C.A.; Steciuk, G.; Jacob, D.; Roussel, P.; Boullay, P.; Klementová, M.; Gemmi, M.; Kopeček, J.; Domeneghetti, M.C.; et al. Structure Refinement Using Precession Electron Diffraction Tomography and Dynamical Diffraction: Tests on Experimental Data. *Acta Crystallogr. Sect. B* **2015**, *71*, 740–751. [[CrossRef](#)]
48. Palatinus, L.; Brázda, P.; Boullay, P.; Perez, O.; Klementová, M.; Petit, S.; Eigner, V.; Zaarour, M.; Mintova, S. Hydrogen Positions in Single Nanocrystals Revealed by Electron Diffraction. *Science* **2017**, *355*, 166–169. [[CrossRef](#)]
49. Brázda, P.; Palatinus, L.; Babor, M. Electron Diffraction Determines Molecular Absolute Configuration in a Pharmaceutical Nanocrystal. *Science* **2019**, *364*, 667–669. [[CrossRef](#)]
50. Klar, P.B.; Krysiak, Y.; Xu, H.; Steciuk, G.; Cho, J.; Zou, X.; Palatinus, L. Accurate Structure Models and Absolute Configuration Determination Using Dynamical Effects in Continuous-Rotation 3D Electron Diffraction Data. *Nat. Chem.* **2023**, *15*, 848–855. [[CrossRef](#)]
51. Palatinus, L.; Brázda, P.; Jelínek, M.; Hrdá, J.; Steciuk, G.; Klementová, M. Specifics of the Data Processing of Precession Electron Diffraction Tomography Data and Their Implementation in the Program PETS2.0. *Acta Crystallogr. Sect. B Struct. Sci. Cryst. Eng. Mater.* **2019**, *75*, 512–522. [[CrossRef](#)]
52. Le Page, Y.; Gabe, E.J.; Gainsford, G.J. A Robust Alternative to  $\eta$  Refinement for Assessing the Hand of Chiral Compounds. *J. Appl. Crystallogr.* **1990**, *23*, 406–411. [[CrossRef](#)]
53. Iwasaki, H.; Sugawara, Y.; Adachi, T.; Morimoto, S.; Watanabe, Y. Structure of 6-O-Methylerythromycin A (Clarithromycin). *Acta Crystallogr. C* **1993**, *49*, 1227–1230. [[CrossRef](#)]
54. Tian, J.; Thallapally, P.K.; Dalgarno, S.J.; Atwood, J.L. Free Transport of Water and CO<sub>2</sub> in Nonporous Hydrophobic Clarithromycin Form II Crystals. *J. Am. Chem. Soc.* **2009**, *131*, 13216–13217. [[CrossRef](#)]
55. de la Cruz, M.J.; Hattne, J.; Shi, D.; Seidler, P.; Rodriguez, J.; Reyes, F.E.; Sawaya, M.R.; Cascio, D.; Weiss, S.C.; Kim, S.K.; et al. Atomic-Resolution Structures from Fragmented Protein Crystals with the CryoEM Method MicroED. *Nat. Methods* **2017**, *14*, 399–402. [[CrossRef](#)] [[PubMed](#)]
56. Blum, T.B.; Housset, D.; Clabbers, M.T.B.; van Genderen, E.; Bacia-Verloop, M.; Zander, U.; McCarthy, A.A.; Schoehn, G.; Ling, W.L.; Abrahams, J.P. Statistically Correcting Dynamical Electron Scattering Improves the Refinement of Protein Nanocrystals, Including Charge Refinement of Coordinated Metals. *Acta Crystallogr. Sect. Struct. Biol.* **2021**, *77*, 75–85. [[CrossRef](#)]
57. Karakulina, O.M.; Demortière, A.; Dachraoui, W.; Abakumov, A.M.; Hadermann, J. In Situ Electron Diffraction Tomography Using a Liquid-Electrochemical Transmission Electron Microscopy Cell for Crystal Structure Determination of Cathode Materials for Li-Ion Batteries. *Nano Lett.* **2018**, *18*, 6286–6291. [[CrossRef](#)]
58. Batuk, M.; Vandemeulebroucke, D.; Ceretti, M.; Paulus, W.; Hadermann, J. Topotactic Redox Cycling in SrFeO<sub>2.5+ $\delta$</sub>  Explored by 3D Electron Diffraction in Different Gas Atmospheres. *J. Mater. Chem. A* **2022**, *11*, 213–220. [[CrossRef](#)]
59. Wu, S.; Li, J.; Ling, Y.; Sun, T.; Fan, Y.; Yu, J.; Terasaki, O.; Ma, Y. In Situ Three-Dimensional Electron Diffraction for Probing Structural Transformations of Single Nanocrystals. *Chem. Mater.* **2022**, *34*, 8119–8126. [[CrossRef](#)]
60. Clabbers, M.T.B.; Xu, H. Microcrystal Electron Diffraction in Macromolecular and Pharmaceutical Structure Determination. *Drug Discov. Today Technol.* **2020**, *37*, 93–105. [[CrossRef](#)]
61. Yang, T.; Waitschat, S.; Inge, A.K.; Stock, N.; Zou, X.; Xu, H. A Comparison of Structure Determination of Small Organic Molecules by 3D Electron Diffraction at Cryogenic and Room Temperature. *Symmetry* **2021**, *13*, 2131. [[CrossRef](#)]
62. Kirkland, E.J. Computation in Electron Microscopy. *Acta Crystallogr. Sect. Found. Adv.* **2016**, *72*, 1–27. [[CrossRef](#)]
63. Seto, Y.; Ohtsuka, M. *Recipro*: Free and Open-Source Multipurpose Crystallographic Software Integrating a Crystal Model Database and Viewer, Diffraction and Microscopy Simulators, and Diffraction Data Analysis Tools. *J. Appl. Crystallogr.* **2022**, *55*, 397–410. [[CrossRef](#)]
64. Cleverley, A.; Beanland, R. Modelling Fine-Sliced Three Dimensional Electron Diffraction Data with Dynamical Bloch-Wave Simulations. *IUCr* **2023**, *10*, 118–130. [[CrossRef](#)] [[PubMed](#)]

65. Dušek, M.; Petříček, V.; Palatinus, L.; Rohlíček, J.; Fejfarová, K.; Eigner, V.; Kučeráková, M.; Poupon, M.; Henriques, M.; Plášil, J.; et al. *Jana2006 Cookbook*; Institute of Physics ASCR, v.v.i.: Prague, Czech Republic, 2019.
66. McMullan, G.; Cattermole, D.M.; Chen, S.; Henderson, R.; Llopart, X.; Summerfield, C.; Tlustos, L.; Faruqi, A. Electron Imaging with Medipix2 Hybrid Pixel Detector. *Ultramicroscopy* **2007**, *107*, 401–413. [[CrossRef](#)] [[PubMed](#)]
67. Delgadillo, D.; Burch, J.; Kim, L.J.; de Moraes, L.; Niwa, K.; Williams, J.; Tang, M.; Lavallo, V.; Chhetri, B.; Jones, C.; et al. High-Throughput Identification of Crystalline Natural Products from Crude Extracts Enabled by Microarray Technology and MicroED. *chemRxiv* **2023**. [[CrossRef](#)]
68. Lightowler, M.; Li, S.; Ou, X.; Cho, J.; Li, A.; Hofer, G.; Xu, J.; Yang, T.; Zou, X.; Lu, M.; et al. Phase Identification and Discovery of Hidden Crystal Forms in a Polycrystalline Pharmaceutical Sample Using High-Throughput 3D Electron Diffraction. *chemRxiv* **2023**. [[CrossRef](#)]
69. Luo, Y.; Wang, B.; Smeets, S.; Sun, J.; Yang, W.; Zou, X. High-Throughput Phase Elucidation of Polycrystalline Materials Using Serial Rotation Electron Diffraction. *Nat. Chem.* **2023**, *15*, 483–490. [[CrossRef](#)]
70. Unge, J.; Lin, J.; Weaver, S.J.; Her, A.S.; Gonen, T. Autonomous MicroED Data Collection Enables Compositional Analysis. *ChemRxiv* **2023**. [[CrossRef](#)]
71. Gillman, C.; Nicolas, W.J.; Martynowycz, M.W.; Gonen, T. Design and Implementation of Suspended Drop Crystallization. *IUCr* **2023**, *10*, 430–436. [[CrossRef](#)] [[PubMed](#)]
72. Martynowycz, M.W.; Shiriaeva, A.; Clabbers, M.T.B.; Nicolas, W.J.; Weaver, S.J.; Hattne, J.; Gonen, T. A Robust Approach for MicroED Sample Preparation of Lipidic Cubic Phase Embedded Membrane Protein Crystals. *Nat. Commun.* **2023**, *14*, 1086. [[CrossRef](#)]
73. Ling, Y.; Sun, T.; Guo, L.; Si, X.; Jiang, Y.; Zhang, Q.; Chen, Z.; Terasaki, O.; Ma, Y. Atomic-Level Structural Responsiveness to Environmental Conditions from 3D Electron Diffraction. *Nat. Commun.* **2022**, *13*, 6625. [[CrossRef](#)]
74. Smeets, S.; Zou, X.; Wan, W. Serial Electron Crystallography for Structure Determination and Phase Analysis of Nanocrystalline Materials. *J. Appl. Crystallogr.* **2018**, *51*, 1262–1273. [[CrossRef](#)] [[PubMed](#)]
75. Wang, B.; Zou, X.; Smeets, S. Automated Serial Rotation Electron Diffraction Combined with Cluster Analysis: An Efficient Multi-Crystal Workflow for Structure Determination. *IUCr* **2019**, *6*, 854–867. [[CrossRef](#)] [[PubMed](#)]
76. Bücker, R.; Hogan-Lamarre, P.; Mehrabi, P.; Schulz, E.C.; Bultema, L.A.; Gevorkov, Y.; Brehm, W.; Yefanov, O.; Oberthür, D.; Kassier, G.H.; et al. Serial Protein Crystallography in an Electron Microscope. *Nat. Commun.* **2020**, *11*, 996. [[CrossRef](#)] [[PubMed](#)]
77. Gorelik, T.E.; Lukat, P.; Kleeberg, C.; Blankenfeldt, W.; Müller, R. Molecular Replacement for Small Molecule Crystal Structure Determination from Electron Diffraction Data with Reduced Resolution. *Acta Cryst. A* **2023**. *submitted*.
78. Gorelik, T.E.; Neder, R.; Terban, M.W.; Lee, Z.; Mu, X.; Jung, C.; Jacob, T.; Kaiser, U. Towards Quantitative Treatment of Electron Pair Distribution Function. *Acta Crystallogr. Sect. B Struct. Sci. Cryst. Eng. Mater.* **2019**, *75*, 532–549. [[CrossRef](#)]
79. Poppe, R.; Vandemeulebroucke, D.; Neder, R.B.; Hadermann, J. Quantitative Analysis of Diffuse Electron Scattering in the Lithium-Ion Battery Cathode Material  $\text{Li}_{1.2}\text{Ni}_{0.13}\text{Mn}_{0.54}\text{Co}_{0.13}\text{O}_2$ . *IUCr* **2022**, *9*, 695–704. [[CrossRef](#)]
80. Gruza, B.; Chodkiewicz, M.L.; Krzeszczakowska, J.; Dominiak, P.M. Refinement of Organic Crystal Structures with Multipolar Electron Scattering Factors. *Acta Crystallogr. Sect. Found. Adv.* **2020**, *76*, 92–109. [[CrossRef](#)]

**Disclaimer/Publisher's Note:** The statements, opinions and data contained in all publications are solely those of the individual author(s) and contributor(s) and not of MDPI and/or the editor(s). MDPI and/or the editor(s) disclaim responsibility for any injury to people or property resulting from any ideas, methods, instructions or products referred to in the content.